Received February 2, 2020, accepted April 18, 2020, date of publication April 23, 2020, date of current version May 8, 2020.

Digital Object Identifier 10.1109/ACCESS.2020.2990083

Passive Generation of the Multi-Wavelength Parabolic Pulses in Tapered Silicon Nanowires

CHAO MEI[1], (Member, IEEE), JINHUI YUAN[1], (Senior Member, IEEE), FENG LI[3], (Member, IEEE), XIAN ZHOU[1], QIANG WU[4,5], BINBIN YAN[2], KUIRU WANG[2], KEPING LONG[1], (Senior Member, IEEE), GERALD FARRELL[6], AND CHONGXIU YU[2]

[1]Research Center for Convergence Networks and Ubiquitous Services, University of Science & Technology Beijing, Beijing 100083, China
[2]State Key Laboratory of Information Photonics and Optical Communications, Beijing University of Posts and Telecommunications, Beijing 100876, China
[3]Photonics Research Centre, Department of Electronic and Information Engineering, The Hong Kong Polytechnic University, Hong Kong
[4]Department of Physics and Electrical Engineering, Northumbria University, Newcastle upon Tyne NE1 8ST, U.K.
[5]Key Laboratory of Nondestructive Test, Ministry of Education, Nanchang Hangkong University, Nanchang 330063, China
[6]Photonics Research Centre, Dublin Institute of Technology, Dublin 2, D08 X622, Ireland

Corresponding authors: Jinhui Yuan (yuanjinhui81@bupt.edu.cn) and Qiang Wu (qiang.wu@northumbria.ac.uk)

This work was supported in part by the National Natural Science Foundation of China under Grant 61875238, and in part by the Research Grant Council of the Hong Kong under Grant PolyU152144/15E.

ABSTRACT In this paper, passive generation of the multi-wavelength parabolic pulses (PPs) in tapered silicon nanowires (TSNs) is numerically investigated. The coupled inhomogeneous nonlinear Schrödinger equation (INLSE) is derived in the context of TSN to model the multi-wavelength PP generation. The TSN is designed based on the well-known self-similar theory that the group-velocity dispersion is decreased while the nonlinear coefficient is unchanged along the propagative direction. While the pump wavelengths for three input pulses are specially set with equal intervals of 18, 12, and 6 nm, the time-domain profiles are aligned at the same position. Simulation results show that except for wavelength interval, the waveguide length is also a critical factor that influences the quality of generated PP. Both of them reshape the pulse profile by the means of walk-off effect which depends on the cross-phase modulation between multiple pulses. By properly optimizing the input parameters of Gaussian pulses as well as the center wavelength interval and TSN length, we prove that the generation of two- even three-wavelength PPs with high-quality is feasible.

INDEX TERMS Multi-wavelength parabolic pulses, self-similar theory, tapered silicon nanowires.

I. INTRODUCTION

Parabolic pulse (PP) generation has been extensively investigated in recent years [1]–[5]. The most important characteristic of PP is that its initial Gaussian form can be retained along the propagation in an optical medium with normal dispersion [6]. For this reason, PP exhibits important applications in high-power lasers [7], [8], high-speed optical communication systems [9], [10] where pulse split needs to be avoided. Up to now, PP could be acquired both from the active fibers [2] and passive media [11] when the input pulse profiles are arbitrary. Specially, PP generation has been experimentally verified in the ytterbium-doped [12]–[14], erbium-doped [15] and Raman fiber amplifiers [16]. In contrast, PP generation in a passive medium attract much less attention because the peak power is gradually reduced in the process of PP formation due to the power diffusion in the normal dispersion region. This property limits its application in which the high power is needed. However, compared to active medium, the passive medium shows two advantages in PP generation. First, the limitation of gain bandwidth [17] which often lead to pulse deformation do not exist for passive media. Second, passive medium is more beneficial to PP generation when the transverse size of used medium has to be lessened to nanometer scale.

On the other hand, on-chip nonlinear optics including pulse compression [18]–[20], supercontinuum generation [21], and optical frequency comb [22]–[24] have been attracting extensive attention. The used optical materials mainly include silicon, chalcogenide, and silicon nitride, etc. Among them, the

The associate editor coordinating the review of this manuscript and approving it for publication was Md. Selim Habib.

silicon-based waveguide demonstrates its superiority in three aspects: strong third-order nonlinear response, large refractive index difference between the waveguide and substrate, and good compatibility with complementary metal oxide semiconductor (CMOS) technology [25]. Nonlinear optical effects such as self-phase modulation (SPM) [26], [27], cross-phase modulation (XPM) [28]–[30], Raman amplification [31], [32], and four-wave mixing [33]–[35] have already been studied in silicon nanowires. Recently, nonlinear dynamics in silicon nanowires referring to PP generation from Gaussian input [36], [37], pulse collisions between two PPs [38], and self-similar propagation and compression of PP [39] are demonstrated. Nevertheless, these work only deal with the situation of single-wavelength PP generation, which in fact puts restriction to PP application especially in the dense wavelength division multiplexing and all-optical signal processing systems. For example, in Ref. [4], although the speed of regenerative wavelength converter based on single-wavelength similariton generation can be up to 40 Gbit/s, the transmission rate is actually limited by ghost pulses. The scheme of two-wavelength PP generation is expected to solve this problem through the dual-channel multiplexing. The transmission rate can be improved to 80 Gbit/s without performance degradation. This indicates the importance of multi-wavelength PP generation in the optical telecommunication. Physically speaking, the fundamental difference between single-wavelength and multi-wavelength PP generations exists in following two aspects. First, the XPM between multi-wavelength pulses could cause significant power redistribution. As a result, the pulse asymmetry in the time domain [40]–[42] can be observed. Second, the multi-wavelength pulses may suffer from free-carrier absorption (FCA) more seriously than the single-wavelength case due to the larger pulse energy within telecommunication waveband launched into silicon nanowires [43], [44].

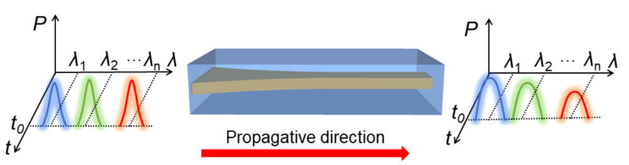

FIGURE 1. Conceptual diagram of the multi-wavelength PP generation in a TSN from input with arbitrary profiles at different center wavelengths.

In this paper, the theoretical model for multi-wavelength PP generation is derived. With our theoretical model, the two-wavelength and three-wavelength PP generations in the tapered silicon nanowires (TSNs) are numerically investigated. The pump pulse parameters as well as waveguide length are properly adjusted to optimize the quality of generated PP. The conceptual illustration of the multi-wavelength PP generation is shown in Fig. 1. It shows multiple Gaussian pulses with different center wavelengths but the same temporal position are launched into the TSN. After propagation, they finally evolve to PPs.

This paper is arranged as follows. In section II, the theoretical model of coupled inhomogeneous nonlinear Schrödinger equation (INLSE) is derived. In section III, TSNs are designed based on the self-similar theory when different waveguide lengths are considered. Simulation results of the two- and three-wavelength PP generations are demonstrated in section IV. In section V, we draw the conclusions.

II. MULTIPLE COUPLED INHOMOGENEOUS NONLINEAR SCHRÖDINGER EQUATION

The nonlinear dynamics of multiple pulses propagating in a TSN can be described by the coupled INLSE as [45]

$$\begin{aligned} i\frac{\partial u_j}{\partial z} &= -\sum_{n=1}^{6}\frac{i^n\beta_n(z)}{n!}\frac{\partial^n u_j}{\partial t^n} - \frac{ic\kappa_j(z)}{2nv_{g,j}(z)}\left[\alpha_l + \alpha_{FC}^j(z)\right]u_j \\ &\quad -\frac{\omega_j\kappa_j(z)}{nv_{g,j}(z)}\delta n_{FC}^j(z)\,u_j - \left[\gamma_j|u_j|^2 + \rho\gamma_{kj}\sum_{j\neq k}^{M}|u_k|^2\right]u_j, \end{aligned} \tag{1}$$

where $u_j(z,t)$ and $u_k(z,t)$ are the two carrier envelop of the slow-varying electric field, z is the propagation distance, t is the retarded time, β_n is the dispersion coefficient which is calculated up to six order in the simulation, c is the speed of light in vacuum, and κ_j is the spatial overlap factor describing the ratio between optical mode field and whole cross-section of the waveguide, which is defined as [29]

$$\kappa_j = \frac{n^2\int_{A_0}\left|e\left(r_t;\omega_j\right)\right|^2 dA}{\int_{A_\infty} n^2(r_t)\left|e\left(r_t;\omega_j\right)\right|^2 dA}, \tag{2}$$

where n is the refractive index of the guiding layer and $n \approx 3.48$ at wavelength of 1550 nm for silicon, $n(r_t)$ is the equivalent refractive index over the whole cross-section, A_0 and A_∞ denote the transversal areas of guiding layer and whole waveguide, respectively. The $v_{g,j}$ in Eq. (1) represents the group velocity of u_j, $\alpha_l = 1$ dB/cm is the linear loss [46], and α_{FC} is the loss induced by FCA, ω is the angular frequency, and δn_{FC} is the change of refractive index induced by the strong field, which gives rise to the free-carrier dispersion (FCD). In the case of multi-pulse propagation in the TSN, FCA and FCD are jointly determined by the total peak power. Following the definitions of α_{FC} and δn_{FC} in the single-pulse case [36], we delimit the α_{FC} and δn_{FC} for multiple co-propagation pulses as

$$\begin{aligned} \alpha_{FC}^j(z) &= \frac{e^3}{n\varepsilon_0 c}\left(\frac{1}{\mu_e m_{ce}^{*2}} + \frac{1}{\mu_h m_{ch}^{*2}}\right) \\ &\quad \times\left[\frac{N_j(z)}{\omega_j^2} + \sum_{k\neq j}^{M}\frac{N_{kj}(z)}{\omega_j\omega_k}\right], \end{aligned} \tag{3}$$

$$\delta n_{\mathrm{FC}}^{j}(z) = \frac{-e^2}{2n\varepsilon_0}\left(\frac{1}{m_{\mathrm{ce}}^*}+\frac{1}{m_{\mathrm{ch}}^*}\right)\left[\frac{N_j(z)+N_j(z)^{0.8}}{\omega_j^2} + \sum_{k\neq j}^{M}\frac{N_{kj}(z)+N_{kj}(z)^{0.8}}{\omega_j\omega_k}\right], \tag{4}$$

where e is the electronic value, ε_0 is the dielectric constant in vacuum. $m_{\mathrm{ce}}^* = 0.26\ m_0$ and $m_{\mathrm{ch}}^* = 0.39\ m_0$ are the effective mass of the electron and hole, respectively where m_0 is the electronic mass. The amounts of generated electron and hole are assumed to be the same, μ_{e} and μ_{h} are the mobility of the electron and hole, respectively. In Eqs. (3) and (4), $k = 1, 2, 3, \ldots, M$ and $k \neq j$. While both N_j and N_{kj} define the densities of free carriers. The SPM-induced N_j is proportional to $|u_j|^4$ while the XPM-induced N_{kj} is proportional to $2|u_j u_k|^2$. This means the free-carrier amount depends on all injected pulses. The total amount of free-carrier density is given as

$$N = \sum_{j}^{M} N_j + \sum_{j\neq k}^{M}\left(N_{jk}+N_{kj}\right). \tag{5}$$

Similar to the equation which describes the free-carrier density in single-pulse case [27], the variation of free-carrier density for the multi-pulse case is represented as

$$\frac{\partial N}{\partial t} = -\frac{N}{t_c} + \frac{3}{4\varepsilon_0 \hbar A_0^2(z)}\left[\sum_{j}^{M}\frac{\Gamma_j''(z)}{v_{g,j}^2(z)}|u_j|^4 + 2\rho\sum_{j\neq k}^{M}\frac{\omega_j\Gamma_{kj}''(z)+\omega_k\Gamma_{jk}''(z)}{(\omega_j+\omega_k)\,v_{g,j}(z)\,v_{g,k}(z)}\left|u_j u_k\right|^2\right], \tag{6}$$

where $t_{\mathrm{c}} \sim 0.5$ ns is the lifetime of free carrier [47]. Γ_j'' is the imaginary part of effective third-order susceptibility of Γ_j for u_j, Γ_j is defined by the certain weighted integrals of the corresponding tensor susceptibilities between the cross-section of the guiding layer and whole transversal area, which is given by [29]

$$\Gamma_j = \frac{A_0\int_{A_0} e_j^*\cdot\chi^{(3)}\vdots e_j e_j^* e_j \mathrm{d}A}{\left[\int_\infty n^2(r_\perp)\left|e_j\right|^2\mathrm{d}A\right]^2}. \tag{7}$$

Γ_{jk}'' in Eq. (6) is the imaginary part of Γ_{jk} which is jointly determined by the distribution of electric fields for u_j and u_k. Γ_{jk} is given by

$$\Gamma_{jk} = \frac{A_0\int_{A_0} e_k^*\cdot\chi^{(3)}\vdots e_j e_j^* e_k \mathrm{d}A}{\left[\int_\infty n^2(r_\perp)\left|e_j\right|^2\mathrm{d}A\int_\infty n^2(r_\perp)\left|e_k\right|^2\mathrm{d}A\right]}. \tag{8}$$

The parameter ρ in both Eqs. (1) and (6) is with the value of 2 when all waves propagating in the TSN are linearly polarized [45], $\chi^{(3)}$ in Eq. (8) can be calculated from the following two equations once the nonlinear refractive n_2 and two photon absorption(TPA) coefficient, β_{TPA}, are obtained.

$$n_2 = 3\chi'^{(3)}\Big/\left(4\varepsilon_0 c n^2\right), \tag{9}$$

$$\beta_{\mathrm{TPA}} = 3\omega\chi''^{(3)}\Big/\left(2\varepsilon_0 c^2 n^2\right). \tag{10}$$

The values of n_2 and β_{TPA} have been experimentally measured and numerically fitted within a wavelength range from 1.3 to 6.2 μm [46]. Therefore, the effective third-order susceptibilities of Γ_j and Γ_{jk} can be also acquired within this wavelength range. Finally, the nonlinear coefficients γ_j and γ_{jk} in Eq. (1) can be obtained by following two equations.

$$\gamma_j(\omega_j, z) = \frac{3\omega_j\Gamma_j(\omega_j, z)}{4\varepsilon_0 A_0(z)\, v_{g,j}^2(\omega_j, z)}, \tag{11}$$

$$\gamma_{jk}(\omega_j, \omega_k, z) = \frac{3\omega_k\Gamma_{jk}(\omega_j, \omega_k, z)}{4\varepsilon_0 A_0(z)\, v_{g,k}(\omega_k, z)\, v_{g,j}(\omega_j, z)}. \tag{12}$$

From Eqs. (11) and (12), it should be noted that both values of γ_j and γ_{jk} depend on z and ω. This in fact indicates that the nonlinear dynamics of pulse shaping for different center wavelengths and TSN profiles should be different, which will be demonstrated in the following sections.

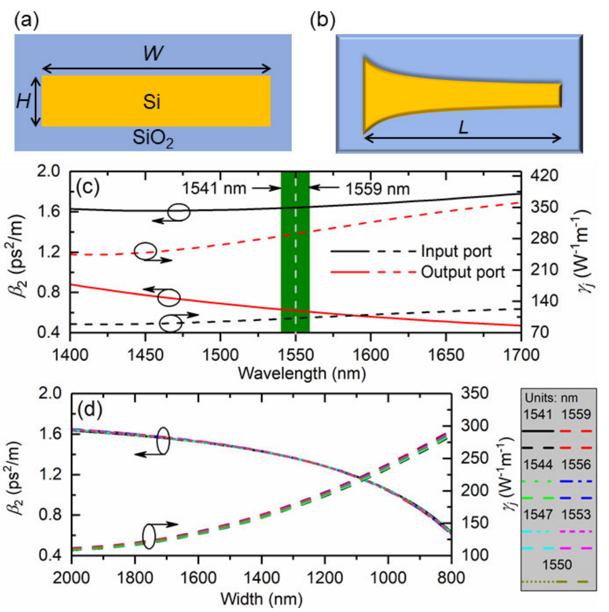

FIGURE 2. (a) The cross-section and (b) top view of the silicon nanowire, (c) β_2 as a function of wavelength at the input (black solid curve) and output (red solid curve) ports, γ_j as a function of wavelength at the input (black dashed curve) and output (red dashed curve) ports, the white dashed line indicates the wavelength of 1550 nm, the green bar represents the wavelength range considered, and (d) the variations of β_2 and γ_j as functions of W for wavelengths 1541 and 1559, 1544 and 1566, 1547 and 1553, and 1550 nm.

III. WAVEGUIDE DESIGN AND DETERMINATION OF WAVEGUIDE LENGTH

A. WAVEGUIDE DESIGN BASED ON THE SELF-SIMILAR THEORY

In this subsection, the TSN design based on self-similar theory is discussed since according to self-similar theory, the PP generation can be ensured. Figure 2(a) shows the cross-section of designed TSN. The guided layer of silicon is buried in the SiO2 cladding. Because of the large refractive index difference between the silicon (~3.48) and SiO_2 (~1.44), the optical field at 1550 nm can be well confined in the guiding layer [19]. The buried structure is chosen because it contributes to the end coupling in practice implementation. The silicon nanowire is tapered along the propagation direction and forms the TSN, as shown in Fig. 2(b). The widths (W) for the TSN are 2000 and 800 nm at the input and output ports, respectively. The height (H) is fixed at 220 nm. By using the finite element method, the group-velocity dispersion (GVD) parameter β_2 at the input and output ports are calculated as a function of wavelength ranging from 1400 to 1700 nm, as shown in Fig. 2(c). The white dashed line indicates the position of 1550 nm and the green bar represents the wavelength range from 1541 to 1559 nm which we are interested in this work. It can be seen from Fig. 2(c) that β_2 at the input port is increased as wavelength. Instead, it is decreased as wavelength at the output port. The values of γ_j at both input and output ports are increased as wavelength. The exact value at 1550 nm for β_2 are 1.64 and 0.62 ps^2/m, and γ_j are 102.3 and 290.8 W^{-1}m^{-1} at the input and output ports, respectively. Six input Gaussian pulses are divided into three groups according to different center wavelengths. In the case of two wavelengths, the three groups are located at 1541 and 1559 nm, 1544 and 1556 nm, and 1547 and 1553 nm, respectively. In the case of three wavelengths, the three groups are located at 1541, 1550 and 1559 nm, 1544, 1550 and 1556 nm, and 1547, 1550 and 1553 nm, respectively. Figure 2(d) shows the variations of β_2 and γ_j as function of W. It can be seen that the slope of β_2 is slightly increased when W is reduced, which indicates that the group-velocity mismatch gradually increases along propagation. However, all curves for β_2 and γ_j at different center wavelengths almost coincide with each other. This means all input pulses will show similar evolving trace in the designed TSN. Although there are three methods can be found to design TSN according to self-similar theory [39], we choose the widely used one that β_2 is decreased and γ_j is a constant along z. This method can be mathematically described as [37]

$$\beta_2(z) = \frac{\beta_{20}}{1 + g_{eq} z}, \tag{13a}$$

$$\gamma_j(z) = \gamma_0, \tag{13b}$$

where β_{20} is the value of β_2 at $z = 0$, $g_{eq} > 0$ is the equivalent gain constant depending on the TSN profile, γ_0 is the value of γ_j at $z = 0$. Equation (13b) clearly indicates that the nonlinear coefficient is kept as a constant over the whole propagation.

The variations of W, β_2, and γ_j along z are plotted in Fig. 3. In Fig. 3(a), W is decreased with z when the waveguide length $L = 0.5$, 1 and 2 mm, respectively. These curves in Fig. 3(a) offer theoretical guidance for practical waveguide fabrication. Figures 3(b), 3(c), and 3(d) show the variations of β_2 and γ_j when $L = 0.5$, 1 and 2 mm, respectively. From Figs. 3(b) to 3(d), L and β_2 are decreased but γ_j is increased with z, which indicates that the self-similar evolution is possible in this TSN. However, the rate of self-similar evolution for

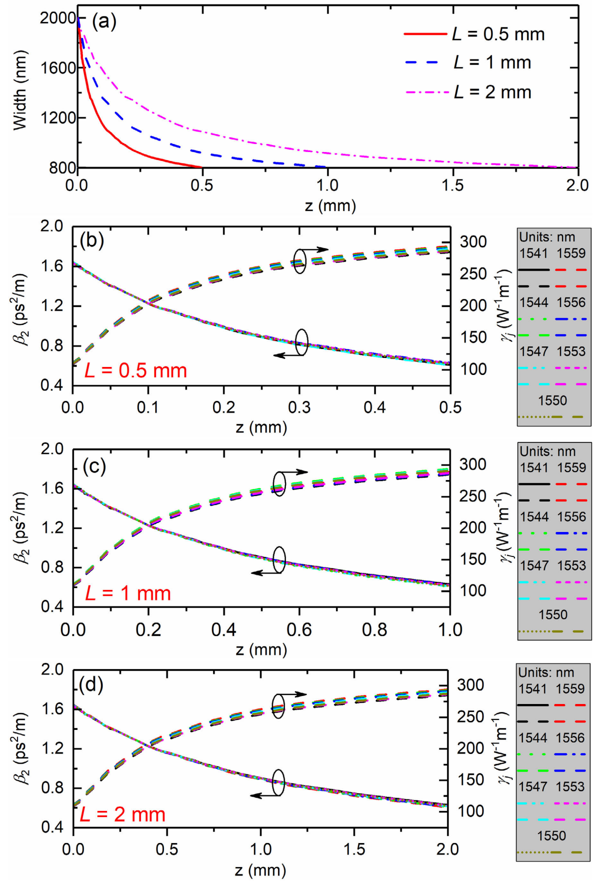

FIGURE 3. (a) The variation of W along z when L is chosen as 0.5 (red solid curve), 1 (blue dashed curve), and 2 mm (pink dashed dot curve), and the variation of β_2 and γ_j along z when L is chosen as (a) 0.5, (b) 1, and (c) 2 mm at wavelengths 1541, 1544, 1547, 1550, 1553, 1556, and 1559 nm.

different L is slightly different. As the curves of β_2 and γ_j for each wavelength are very close, only the design at 1550 nm is considered for multi-wavelength PP generations. This wavelength is pick up because TSN can support single-wavelength PP generation at 1550 nm when XPM effect is ignored [37]. The XPM-associated L enables us to distinguish the PP generation in single- and multi-wavelength cases. It should be noted that although Eq. (13) provides one approach to design TSN, high-quality PP can be also generated by the means of the other two [39] which we do not discuss here.

B. DETERMINATION OF THE WAVEGUIDE LENGTH

Before determining the suitable L for multi-wavelength PP generation when XPM is presented, we need to evaluate the walk-off effect between the two input pulses for different wavelength assembles. This procedure may help us refrain from the XPM-induced walk-off effect which probably lead to asymmetries of temporal pulse. Assuming both pulse widths are the same as T_0, the walk-off distance L_W can be introduced as [45]

$$L_W = T_0/|\beta_1(\lambda_1) - \beta_1(\lambda_2)|, \tag{14}$$

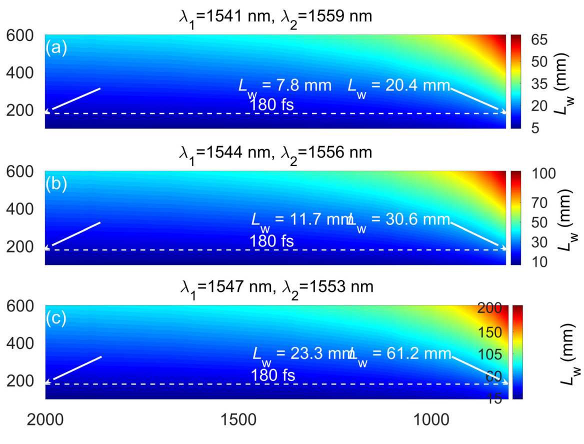

FIGURE 4. The walk-off distances L_W for (a) $\lambda_1 = 1541$ and $\lambda_2 = 1559$ nm, (b) $\lambda_1 = 1544$ and $\lambda_2 = 1556$ nm, and (c) $\lambda_1 = 1547$ and $\lambda_2 = 1553$ nm when T_{FWHM} is increased from 100 to 600 fs and W is changed from 2000 to 800 nm. The white dashed lines represent the location of $T_{FWHM} = 180$ fs, and the maximal and minimal L_W for each white dashed line are 7.8 and 20.4 mm, 11.7 and 30.6 mm, and 23.3 and 61.2 mm in (a), (b), and (c), respectively.

where $\beta_1 = 1/v_g$, λ_1 and λ_2 are center wavelengths for two injected pulses. Figures 4(a) to 4(c) show the calculated L_W for different choices of λ_1 and λ_2. The full width at half maximum (FWHM) of T_{FWHM} is varied from 100 to 600 fs and W is decreased from 2000 to 800 nm in Fig. 4. When $\lambda_1 = 1541$ nm and $\lambda_2 = 1559$ nm, the variation of L_W is shown in Fig. 4(a) in which L_W is reduced when T_{FWHM} is decreased or W is increased. This is because when T_{FWHM} is deceased, the input power will be increased to keep pulse energy as a constant. As a result, nonlinear power coupling takes place after only a short propagation. Besides, β_2 will become larger for the increased W according to Fig. 2(d). Thus, the difference between absolute $\beta_1(\lambda_1)$ and $\beta_1(\lambda_2)$ also becomes larger, which essentially decreases the L_W. The maximal L_W appears at the upper right corner where T_{FWHM} and W show the maximal and minimal values, respectively. Similar pattern can be observed in Figs. 4(b) and 4(c). The difference is that as $\Delta\lambda$ is decreased, both the minimal and maximal values of L_W are increased. For example, when $\Delta\lambda = 18$ nm, the maximal value of L_W is 20.4 mm. However, when $\Delta\lambda = 6$ nm, the maximal value of L_W is 61.2 mm. In order to get rid of the influence from walk-off effect and ensure high-quality PP generation, the condition $L \ll L_W$ should be satisfied in the simulation. From Fig. 4(a), one can clearly deduce that L needs to be shorter than 7.8 mm.

To further reduce the selection range of L, we investigate the temporal evolutions at wavelengths (i) $\lambda_1 = 1541$ and $\lambda_2 = 1559$ nm, (ii) $\lambda_1 = 1544$ and $\lambda_2 = 1556$ nm, and (iii) $\lambda_1 = 1547$ and $\lambda_2 = 1553$ nm in Figs. 5(a), 5(b), and 5(c), respectively. The peak power and width of temporal pulses for the three groups are decreased and increased respectively when z is increased from 0.3 to 3 mm. These variations are regarded as typical features for self-similar evolution in passive media.

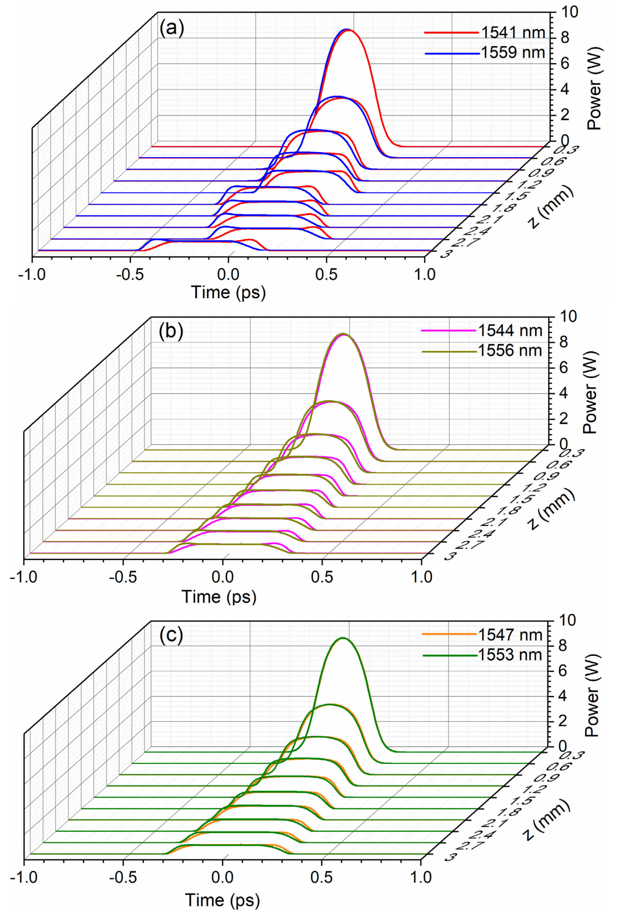

FIGURE 5. The power variation of the temporal pulse along a 3-mm long TSN for (a) $\lambda_1 = 1541$ (red curves) and $\lambda_2 = 1559$ nm (blue curves), (b) $\lambda_1 = 1544$ (pink curves) and $\lambda_2 = 1556$ nm (dark yellow curves), and (c) $\lambda_1 = 1547$ (orange curves) and $\lambda_2 = 1553$ nm (green curves).

Moreover, the temporal separation caused by walk-off effect between each pair of pulses is reduced at the same z when the $\Delta\lambda$ is reduced from Figs. 5(a) to 5(c). Unfortunately, at the end of propagation in the three figures, flat-top pulse appears which indicates the excessively nonlinear phase. This is quite obvious for smaller $\Delta\lambda$. Therefore, it is necessary to control L to prevent the possible redundant nonlinear phase. Another important phenomenon is the drift of center position for temporal pulse, which is oscillating near $t = 0$. This oscillation is believed to origin from the unequal spectral modulation between two propagating pulses. When $\Delta\lambda$ is 12 and 6 nm, the oscillating characteristic almost disappears, as shown in Figs. 5(b) and 5(c). The reason is that the XPM-induced spectral modulation tends to the same, which give rises to the same group velocity for the co-propagating pulse. It concludes from Fig. 5 that as the pulse deformation is proportional to z, L needs to be shorter than 3 mm to ensure high-quality two-wavelength PP generation especially for the worst case of $\Delta\lambda = 18$ nm.

To clearly demonstrate the deviations between output pulse and parabola, comparisons are plotted in Figs. 6(a), 6(b), and 6(c) when $\Delta\lambda = 18$, 12, and 6 nm,

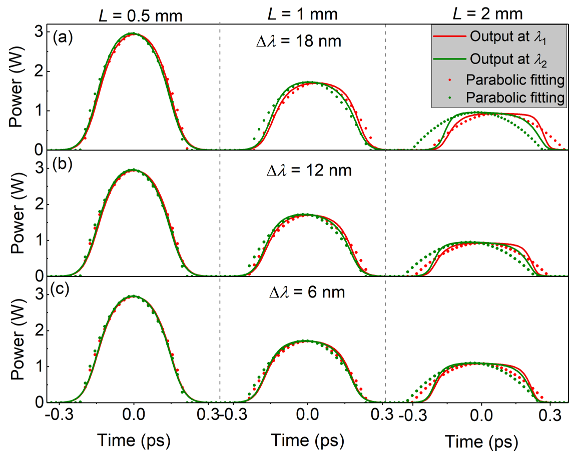

FIGURE 6. **Output pulses from the designed TSNs with length of 0.5, 1, and 2 mm when pump wavelength intervals are (a) $\Delta\lambda = 18$ nm, (b) $\Delta\lambda = 12$ nm, and (c) $\Delta\lambda = 6$ nm. The red solid and green solid curves are the output pulses at λ_1 and λ_2, and the red and green dots are the parabolic fitting of the output pulses at λ_1 and λ_2, respectively.**

respectively. For each $\Delta\lambda$, simulations for the cases of $L = 0.5$, 1 and 2 mm are conducted. The input peak power and T_{FWHM} for all cases are 400 W and 180 fs, respectively. It can be seen from Fig. 6(a) that the output pulses gradually deviate from the parabola due to the excessively accumulated nonlinear phase caused by XPM when L is increased from 0.5 to 2 mm. The most serious deviation happens for the case of $L = 2$ mm because the output pulse is far away from parabolic fitting. As a result, high-quality multi-wavelength PP generation is impossible. Similar scenario can be found in Figs. 6(b) and 6(c). In another aspect, the output pulse is closer to a parabola when $\Delta\lambda$ is reduced from 18 to 6 nm even if $L = 2$ mm, which can be explained by the decreased group-velocity mismatch. It is obvious that compared to $\Delta\lambda$, L plays a more important role in making the output pulse away from desired PP.

As conclusions, we focus on designing TSN and investigating the influence of L as well the wavelength interval on the walk-off effect. It is evident that L acts as a dominant role in affecting the self-similar evolution and PP formation compared to $\Delta\lambda$. Since in previous work [5], the input peak power and T_{FWHM} are proved to affect the PP generation as well in the single-wavelength case. In the following, the optimization of the input peak power and T_{FWHM} in the case of multi-wavelength PP generation will be discussed focally.

IV. SIMULATION RESULTS FOR MILTI-WAVELENGTH PP GENERATIONS

A. TWO-WAVELENGTH PP GENERATION

Same as above, six pulses are divided into three groups as (i) $\lambda_1 = 1541$ and $\lambda_2 = 1559$ nm, (ii) $\lambda_1 = 1544$ and $\lambda_2 = 1556$ nm, and (iii) $\lambda_1 = 1547$ and $\lambda_2 = 1553$ nm in this subsection for two-wavelength PP generation. First, we introduce a mismatch parameter σ to quantality evaluate the quality of generated PP in the single-wavelength case as

$$\sigma^2 = \frac{\int_{-\infty}^{+\infty} \left[P(t) - P_{\mathrm{f}}(t)\right]^2 dt}{\int_{-\infty}^{+\infty} P^2(t)\, dt}, \tag{15}$$

where $P(t)$ and $P_{\mathrm{f}}(t)$ are the powers of output pulse and fitted parabola, respectively. To understand the impacts of input peak power and T_{FWHM} on the two-wavelength PP generation, σ under different input peak powers and T_{FWHM} are calculated when $L = 0.5$, 1, and 2 mm, respectively. The symbol of σ at λ_1 and λ_2 are reset as σ_1 and σ_2. Two new variables are introduced to quantality evaluate the quality of generated PP in the two-wavelength case as

$$\sigma_{\mathrm{sum}}^2 = \sigma_1^2 + \sigma_2^2, \tag{16a}$$

$$\sigma_{\mathrm{diff}}^2 = \left|\sigma_1^2 - \sigma_2^2\right|. \tag{16b}$$

For the minimal value of both σ_{sum} and σ_{diff}, the output two pulses can be very close to PP. The effective mismatch parameter is defined as

$$\sigma_{\mathrm{sd}}^2 = 1000 \times \left(\sigma_{\mathrm{sum}}^2 + \sigma_{\mathrm{diff}}^2\right) \Big/ n_{\mathrm{w}}, \tag{17}$$

where n_{w} is the number of input center wavelengths. For the two-wavelength case, $n_{\mathrm{w}} = 2$. It is clear that smaller value of σ_{sd} means better quality of output two pulses. This definition provides a useful approach to quantality assess the quality of output two pulses with only one parameter.

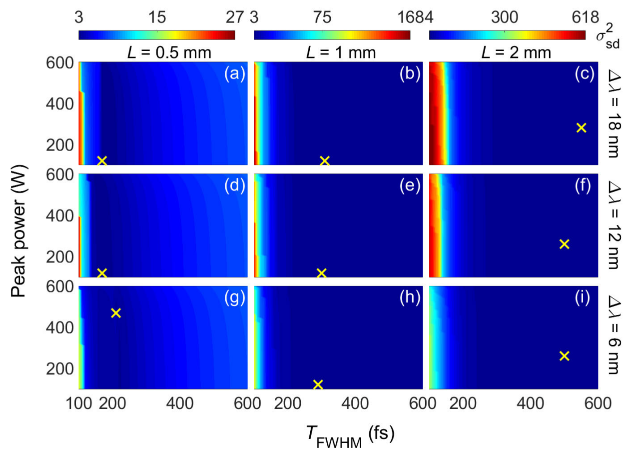

FIGURE 7. **When $\Delta\lambda = 18$ nm, the maps of σ_{sd} for the different peak powers and T_{FWHM} of the input pulses for $L =$ (a) 0.5, (b) 1, and (c) 2 mm. The maps for $L =$ (d) 0.5, (e) 1, and (f) 2 mm when $\Delta\lambda = 12$ nm. The maps for $L =$ (g) 0.5, (h) 1, and (i) 2 mm when $\Delta\lambda = 6$ nm. The yellow crosses represent the location of the minimal σ_{sd}.**

Figure 7 shows the distribution of σ_{sd}^2 when input peak power and T_{FWHM} change from 100 to 600 W and from 100 to 600 fs, respectively. The step sizes in peak power and FWHM are 10 W and 10 fs. The input peak power and T_{FWHM} for two pulses are the same. Figure 7(a) to 7(c) demonstrate that the values of σ_{sd}^2 from 100 to 200 fs are increased with L because of the increased pulse deformation caused by the walk-off effect. Similar scenario can be found from Figs. 7(d) to 7(f) and

Figs. 7(g) to 7(i) in which the $\Delta\lambda$ are 12 and 6 nm, respectively. Yet, the distinction is that the increasing rate for σ_{sd} is slowed down as $\Delta\lambda$ is decreased from 18 to 6 nm. In Figs. 7(a), 7(d), and 7(g) in which the L are fixed at 0.5 mm, σ_{sd} is also decreased as $\Delta\lambda$ is reduced from 18 to 6 nm. In addition, when L is fixed at 1 and 2 mm, the similar trends are observed, which corresponds to Figs. 7(b), 7(e) and 7(h), and Figs. 7(c), 7(f) and 7(i), respectively. All these results point to one fact that smaller $\Delta\lambda$ shows great advantage in self-similar evolution. For the fixed $\Delta\lambda = 18$ nm, the maximal values of σ_{sd}^2 are 27, 168, and 618, and the minimal value of σ_{sd}^2 are 2.9, 3.1 and 3.7 when $L = 0.5$, 1, and 2 mm, respectively. These minimal values are marked by yellow crosses as shown in Fig. 7. It can be seen that suitable input peak power as well T_{FWHM} strongly determine the high-quality multi-wavelength PP generation. The corresponding value of T_{FWHM} for three minimal σ_{sd}^2 are 170, 310, and 550 fs, respectively. It shows longer TSN requires larger T_{FWHM} to achieve high-quality PP for given input peak power.

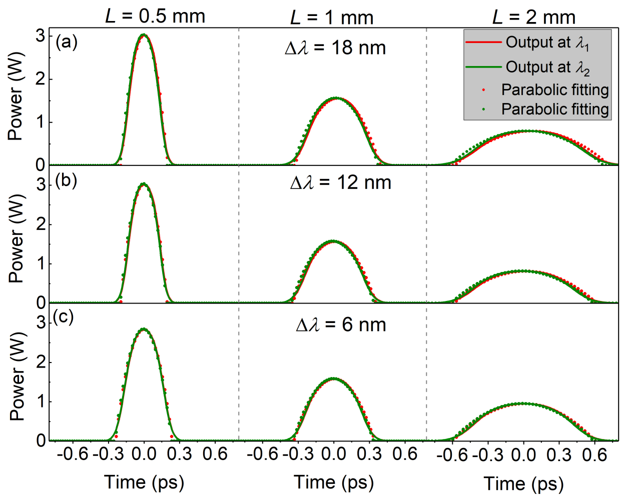

FIGURE 8. The generated PP at the minimal value of σ_{sd}^2 for $L = 0.5$, 1, and 2 mm when (a) $\Delta\lambda = 18$ nm, (b) $\Delta\lambda = 12$ nm, and (c) $\Delta\lambda = 6$ nm. The red and green solid curves represent the output pulses at λ_1 and λ_2, and the red and green dots represent the parabolic fittings of the output pulses at λ_1 and λ_2, respectively.

The exact waveforms and their parabolic fittings for the output two-wavelength pulses at $\Delta\lambda = 18$, 12, and 6 nm are shown in Figs. 8(a), 8(b), and 8(c), respectively. The parabolic fittings are conducted under the condition that the values of σ_{sd}^2 in Fig. 7 are minimal. From Fig. 8, all pulses can be well fitted by the parabolas which means the pulse deformation can be relieved to some extent by matching the XPM, SPM and GVD after optimizing the input peak power and T_{FWHM}. That is to say, the inherent balance between nonlinearity and dispersion required by two-wavelength PP generation is satisfied. Different from the case of single-wavelength PP generation, XPM provides another free degree to control the PP generation in the two-wavelength case. It is evident that the two-wavelength PPs with high quality have been generated by optimizing the input peak power and T_{FWHM} in the TSNs when $L = 0.5$, 1, and 2 mm, respectively.

B. THREE-WAVELENGTH PP GENERATION

For the case of three-wavelength PP generation, the six pump wavelengths are also divided into three groups as (i) $\lambda_1 = 1541$, $\lambda_2 = 1550$ and $\lambda_3 = 1559$ nm, (ii) $\lambda_1 = 1544$, $\lambda_2 = 1550$ and $\lambda_3 = 1556$ nm, and (iii) $\lambda_1 = 1547$, $\lambda_2 = 1550$ and $\lambda_3 = 1553$ nm. The maximal and minimal values of $\Delta\lambda$ in this case are the same as those in the two-wavelength case. However, the nonlinear interaction in the three-wavelength case is more complicated than the two-wavelength one because each optical spectrum will be simultaneously modulated by the other two via XPM. For the three-wavelength case, the quality of generated pulses can be quantality evaluated by following two equations as

$$\sigma_{sum}^2 = \sigma_1^2 + \sigma_2^2 + \sigma_3^2, \tag{18}$$

$$\sigma_{diff}^2 = \left|\sigma_1^2 - \sigma_2^2\right| + \left|\sigma_2^2 - \sigma_3^2\right| + \left|\sigma_1^2 - \sigma_3^2\right|, \tag{19}$$

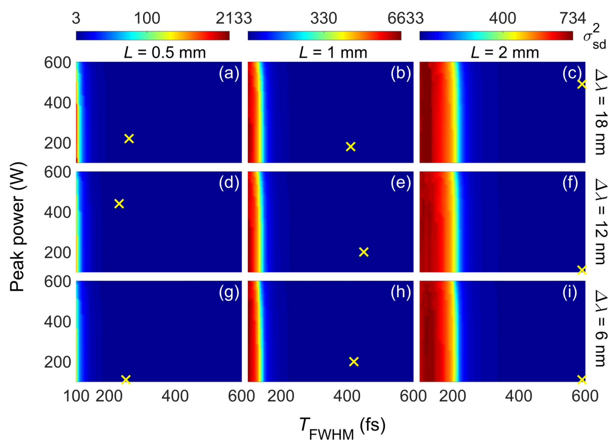

FIGURE 9. When $\Delta\lambda = 18$ nm, the maps of σ_{sd} for the different peak powers and T_{FWHM} of the input pulses for $L =$ (a) 0.5, (b) 1, and (c) 2 mm. The maps for $L =$ (d) 0.5, (e) 1, and (f) 2 mm when $\Delta\lambda = 12$ nm. The maps for $L =$ (g) 0.5, (h) 1, and (i) 2 mm when $\Delta\lambda = 6$ nm. The yellow crosses represent the location of the minimal σ_{sd}.

where σ_1, σ_2, and σ_3 are the mismatch parameters of the three output pulses from one TSN at center wavelengths of λ_1, λ_2, and λ_3, respectively. Similar to the two-wavelength case, σ_{sd} in the three-wavelength case can be calculated after σ_{sum} and σ_{diff} defined by Eqs. (18) and (19) are determined. The calculated distribution of σ_{sd}^2 are shown in Fig. 9 when the input peak power and T_{FWHM} are varied from 100 to 600 W and from 100 to 600 fs, respectively. It can be seen that σ_{sd} is increased with L and decreased with $\Delta\lambda$, which exhibits the same trend as the two-wavelength case in Fig. 7. The first difference manifests in that the maximal value of σ_{sd}^2 in Fig. 9 is 213, but in Fig. 7 it is only 27 when $L = 0.5$ mm. The same situations can be also found for $L = 1$ and 2 mm. Therefore, the quality of generated three-wavelength PPs is worse than that of two-wavelength case. The reason is that the three-wavelength pulses at telecommunication band suffer from stronger nonlinear absorption including the TPA and FCA than that of two-wavelength case in the TSN. It has been proved that TPA allows significantly degradation in quality of generated PPs [37]. Another difference is that the growth rate of $\sigma_{\rm sd}$ from 100 to 200 fs in Fig. 9 is faster than that in Fig. 7 when $L = 0.5$, 1 and 2 mm. This is because the self-similar evolution for three-wavelength case experiences stronger obstruction due to the presence of nonlinear absorption. The positions where the minimal values of $\sigma_{\rm sd}^2$ are located at are marked by yellow crosses, as shown in Figs. 9(a) to 9(i). The corresponding $T_{\rm FWHM}$ for the minimal $\sigma_{\rm sd}^2$ is increased with L increasing from 0.5 to 2 mm. Although most values of $\sigma_{\rm sd}$ for three-wavelength case are larger than that of two-wavelength case, the minimal value of $\sigma_{\rm sd}^2$ for the two cases are almost the same. For example, when $L = 0.5$ mm and $\Delta\lambda = 6$ nm, the minimal $\sigma_{\rm sd}^2$ are 2.89 and 2.95, respectively, which are very close to each other. In a word, the generation of three-wavelength PPs with high quality has been achieved.

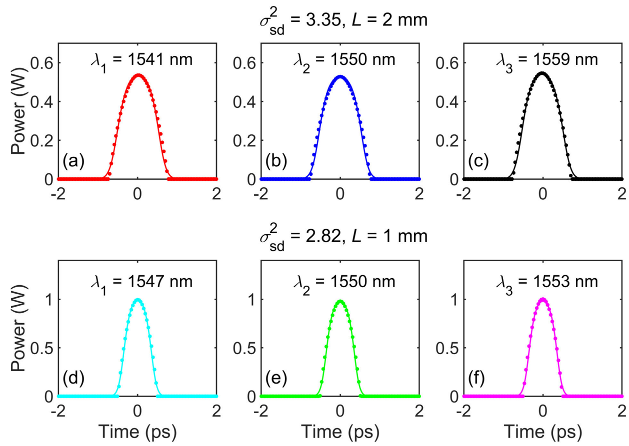

FIGURE 10. When $\sigma_{\rm sd}^2 = 3.35$ and $L = 2$ mm, the output pulses and their parabolic fittings at (a) $\lambda_1 = 1541$, (b) $\lambda_2 = 1550$, and (c) $\lambda_3 = 1559$ nm. When $\sigma_{\rm sd}^2 = 2.82$ and $L = 1$ mm, the output pulses and their parabolic fittings at (d) $\lambda_1 = 1547$, (e) $\lambda_2 = 1550$, and (f) $\lambda_3 = 1553$ nm.

The exact waveform of individual output pulse and its parabolic fitting in the time-domain are shown in Figs. 10(a) to 10(f) for the three-wavelength case. The corresponding values of $\sigma_{\rm sd}^2$ are 3.35 for $L = 2$ mm and 2.82 for $L = 1$ mm. These two values of $\sigma_{\rm sd}^2$ correspond to the maximal and minimal values among all $\sigma_{\rm sd}^2$ marked by yellow crosses in Fig. 9. In Figs. 10(a) to 10(c), the three output pulses are well fitted by its parabolic counterpart at center wavelengths of $\lambda_1 = 1541$, $\lambda_2 = 1550$, and $\lambda 3 = 1559$ nm. However, smaller value of $\sigma_{\rm sd}^2$ in Figs. 10(d) to 10(f) means that the output waveforms under reduced $\Delta\lambda$ are closer to parabolas. This can be attributed to the approximately equal group velocity between the three co-propagating pulses. The corresponding physical mechanism is similar to the two-wavelength case. It should be noted that although only two output waveforms for $L = 2$ mm and 1 mm are shown in Fig. 10, the minimal values of $\sigma_{\rm sd}^2$ in all nine subfigures in Fig. 9 are very close to each other.

TABLE 1. The minimal values of $\sigma_{\rm sd}^2$ for different cases.

L (mm) / $\Delta\lambda$ (nm)	Two-wavelength case			Three-wavelength case		
	0.5	1	2	0.5	1	2
18	2.95	3.08	3.68	2.89	2.87	3.35
12	3.19	3.33	2.99	3.03	2.88	3.12
6	3.27	2.89	2.92	2.86	2.82	3.08

The minimal values of $\sigma_{\rm sd}^2$ for different L and $\Delta\lambda$ are given in Table 1 in order to clearly manifest the quality of generated two-wavelength and three-wavelength PPs. From Table 1, the minimal values of $\sigma_{\rm sd}^2$ for the two-wavelength and three-wavelength cases are 2.89 and 2.82, respectively when $\Delta\lambda = 6$ nm and $L = 1$ mm. However, among all minimal $\sigma_{\rm sd}^2$ marked by yellow crosses in Figs. 7 and 9, the maximal values are 3.68 in Fig. 7 and 3.35 in Fig. 9, respectively. At this time, $\Delta\lambda = 18$ nm and $L = 2$ mm. These results again confirm that both $\Delta\lambda$ and L significantly affect the quality of generated PPs. Therefore, to obtain high-quality multi-wavelength PPs in designed TSN, it is necessary to optimize all parameters including the input peak power and $T_{\rm FWHM}$, as well as the waveguide length L and wavelength interval $\Delta\lambda$.

The time-domain characteristics of output pulses have been demonstrated in above section. Now we will investigate the frequency-domain characteristics which can be measured by the frequency-resolved optical gating (FROG). For this purpose, the time-frequency map is adopted because it can reflect the time-domain as well as frequency-domain information at the same time. The time-frequency map can be described as [48]

$$S(\omega, \tau) = \left| \int_{-\infty}^{\infty} u(t)\, g(t-\tau)\, e^{-i\omega t} \mathrm{d}t \right|^2, \qquad (20)$$

where $g(t-\tau)$ is the variable-delay gate function with a Gaussian shape of 200-fs width and τ is the delayed time. Fig. 11 shows the resulted time-frequency maps in which Figs. 11(a) and 11(b) demonstrate the output S for $L = 2$ mm when λ_1 and λ_2 are chosen as 1541 and 1559 nm, respectively. Figs. 11(c) to 11(e) show the output S for $L = 2$ mm when λ_1, λ_2, and λ_3 are 1541, 1550, and 1559 nm, respectively. Obviously, all optical spectra are stretched around its center wavelength because of the spectral broadening under XPM and SPM. The two ends of stretched spectra are thicker than the middle portions, suggesting higher energy distribution at both ends than the middle portion. This is also indicated from the optical spectra plotted by white solid curves. All spectral curves in Figs. 11(a) to 11(e) have a nearly symmetrical bimodal structure, which is similar to the spectral profile only caused SPM. This allows temporal pulses do not manifest any asymmetric deformation. Furthermore, the spectral intensities in Figs. 11(a) and 11(b) are higher

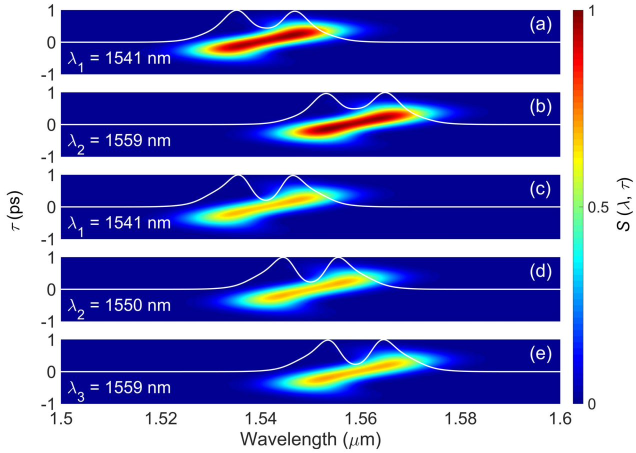

FIGURE 11. The time-frequency maps from a 2-mm long TSN when the pump wavelengths are (a) 1541 nm and (b) 1559 nm for the two-wavelength case, (c) 1541 nm, (d) 1550 nm, and (e) 1559 nm for the three-wavelength case. The white solid curves represent the normalized spectral intensity.

than those in Figs. 11(c) to 11(e) because the two-wavelength pulses are subject to a lower nonlinear absorption than the three-wavelength one. More importantly, the nonlinear absorption not only reduces the output spectral intensity, but also deteriorates the quality of generated multi-wavelength PPs. Further simulation results show that by using suitable optical filters, an individual temporal component for each center wavelength among all output PPs can be perfectly extracted and reproduced.

It should be noted that in this work, although we only show the generation of two-wavelength and three-wavelength PPs, PPs with more than three wavelengths can also be generated with high quality as long as the walk-off effect can be effectively restrained. This can be realized by appropriately optimizing L and $\Delta\lambda$, as well as the input peak power and $T_{\rm FWHM}$. This work provides a general scheme for multi-wavelength PP generation in passive media.

V. CONCLUSIONS

In summary, the theoretical model for multi-wavelength PP generation in designed TSNs is derived. It shows small L and $\Delta\lambda$ can weaken the walk-off effect and improve the quality of generated multi-wavelength PPs. To obtain high-quality multi-wavelength PPs, the maximal values for L and $\Delta\lambda$ are chosen as 2 mm and 18 nm. Simulation results show that two-wavelength and three-wavelength PPs can be generated with high quality after optimizing the input peak power and $T_{\rm FWHM}$ of Gaussian pulses. The minimal values of $\sigma_{\rm sd}^2$ for the two-wavelength and three-wavelength cases are 2.89 and 2.82. for two-wavelength and three-wavelength cases are 2.89 and 2.82, respectively. It is believed that the proposed scheme of multi-wavelength PP generations has important applications in the on-chip dense wavelength division multiplexing and all-optical signal processing systems.

REFERENCES

[1] J. M. Dudley, C. Finot, D. J. Richardson, and G. Millot, "Self-similarity in ultrafast nonlinear optics," *Nature Phys.*, vol. 3, pp. 597–603, Sep. 2007.
[2] M. E. Fermann, V. I. Kruglov, B. C. Thomsen, J. M. Dudley, and J. D. Harvey, "Self-similar propagation and amplification of parabolic pulses in optical fibers," *Phys. Rev. Lett.*, vol. 84, no. 26, pp. 6010–6013, Jun. 2000.
[3] B. K. Ghosh, D. Ghosh, and M. Basu, "Potential use of nonlinearity-induced virtual gain on parabolic pulse formation in highly nonlinear tapered fiber system," *J. Opt.*, vol. 21, no. 4, Apr. 2019, Art. no. 045503.
[4] D. Chowdhury, D. Ghosh, N. Bose, and M. Basu, "Parabolic pulse regeneration in normal dispersion-decreasing fibers and its equivalent substitutes in presence of third-order dispersion," *Appl. Phys. B, Lasers Opt.*, vol. 125, no. 6, p. 106, Jun. 2019.
[5] C. Mei, J. Yuan, F. Li, B. Yan, X. Sang, X. Zhou, Q. Wu, K. Wang, K. Long, and C. Yu, "Generation of parabolic pulse in a dispersion and nonlinearity jointly engineered silicon waveguide taper," *Opt. Commun.*, vol. 448, pp. 48–54, Oct. 2019.
[6] D. Anderson, M. Desaix, M. Karlsson, M. Lisak, and M. L. Quiroga-Teixeiro, "Wave-breaking-free pulses in nonlinear-optical fibers," *J. Opt. Soc. Amer. B, Opt. Phys.*, vol. 10, no. 7, pp. 1185–1190, Jul. 1993.
[7] Z. Liu, Z. M. Ziegler, L. G. Wright, and F. W. Wise, "Megawatt peak power from a mamyshev oscillator," *Optica*, vol. 4, no. 6, pp. 649–654, Jun. 2017.
[8] W. H. Renninger, A. Chong, and F. W. Wise, "Self-similar pulse evolution in an all-normal-dispersion laser," *Phys. Rev. A, Gen. Phys.*, vol. 82, no. 2, Aug. 2010, Art. no. 021805.
[9] C. Finot, S. Pitois, and G. Millot, "Regenerative 40 Gbit wavelength converter based on similariton generation," *Opt. Lett.*, vol. 30, no. 14, pp. 1776–1778, Jul. 2005.
[10] T. Hirooka and M. Nakazawa, "All-optical 40-GHz time-domain Fourier transformation using XPM with a dark parabolic pulse," *IEEE Photon. Technol. Lett.*, vol. 20, no. 22, pp. 1869–1871, Nov. 2008.
[11] T. Hirooka and M. Nakazawa, "Parabolic pulse generation by use of a dispersion-decreasing fiber with normal group-velocity dispersion," *Opt. Lett.*, vol. 29, no. 5, pp. 498–500, Mar. 2004.
[12] D. N. Papadopoulos, Y. Zaouter, M. Hanna, F. Druon, E. Mottay, E. Cormier, and P. Georges, "Generation of 63 fs 41 MW peak power pulses from a parabolic fiber amplifier operated beyond the gain bandwidth limit," *Opt. Lett.*, vol. 32, no. 17, pp. 2520–2522, Sep. 2007.
[13] J. Limpert, T. Schreiber, T. Clausnitzer, K. Zöllner, H.-J. Fuchs, E.-B. Kley, H. Zellmer, and A. Tännermann, "High-power femtosecond yb-doped fiber amplifier," *Opt. Express*, vol. 10, no. 14, pp. 628–638 , Jul. 2002.
[14] T. Schreiber, C. K. Nielsen, B. Ortac, J. Limpert, and A. Tännermann, "Microjoule-level all-polarization-maintaining femtosecond fiber source," *Opt. Lett.*, vol. 31, no. 5, pp. 574–576, Mar. 2006.
[15] H. Liu, Z. Liu, E. S. Lamb, and F. Wise, "Self-similar erbium-doped fiber laser with large normal dispersion," *Opt. Lett.*, vol. 39, no. 4, pp. 1019–1021, Feb. 2014.
[16] C. Aguergaray, D. Méchin, V. Kruglov, and J. D. Harvey, "Experimental realization of a mode-locked parabolic Raman fiber oscillator," *Opt. Express*, vol. 18, no. 8, pp. 8680–8687, Apr. 2010.
[17] D. B. Soh, J. Nilsson, and A. B. Grudinin, "Efficient femtosecond pulse generation using a parabolic amplifier combined with a pulse compressor II finite gain-bandwidth effect," *J. Opt. Soc. Amer. B, Opt. Phys.*, vol. 23, no. 1, pp. 10–19, Jan. 2006.
[18] D. T. H. Tan, A. M. Agarwal, and L. C. Kimerling, "Nonlinear photonic waveguides for on-chip optical pulse compression," *Laser Photon. Rev.*, vol. 9, no. 3, pp. 294–308, May 2015.
[19] D. T. H. Tan, P. C. Sun, and Y. Fainman, "Monolithic nonlinear pulse compressor on a silicon chip," *Nature Commun.*, vol. 1, no. 1, pp. 1–6, Dec. 2010.
[20] D. T. H. Tan, "Optical pulse compression on a silicon chip—Effect of group velocity dispersion and free carriers," *Appl. Phys. Lett.*, vol. 101, no. 21, Nov. 2012, Art. no. 211112.
[21] Y. Yu, X. Gai, P. Ma, D. Y. Choi, Z. Yang, R. Wang, and B. L. Davies, "A broadband, quasi continuous, mid infrared supercontinuum generated in a chalcogenide glass waveguide," *Laser Photon. Rev*, vol. 8, no. 5, pp. 792–798, Jun. 2014.
[22] M. A. Foster, J. S. Levy, O. Kuzucu, K. Saha, M. Lipson, and A. L. Gaeta, "Silicon-based monolithic optical frequency comb source," *Opt. Express*, vol. 19, no. 15, pp. 14233–14239, Jul. 2011.

[23] P. Del'Haye, A. Schliesser, O. Arcizet, T. Wilken, R. Holzwarth, and T. J. Kippenberg, "Optical frequency comb generation from a monolithic microresonator," *Nature*, vol. 450, no. 7173, pp. 1214–1217, Dec. 2007.

[24] V. Brasch, M. Geiselmann, T. Herr, G. Lihachev, M. H. Pfeiffer, M. L. Gorodetsky, and T. J. Kippenberg, "Photonic chip-based optical frequency comb using soliton Cherenkov radiation," *Science*, vol. 351, no. 6271, pp. 357–360, Jan. 2016.

[25] B. Kuyken, F. Leo, S. Clemmen, U. Dave, R. Van Laer, T. Ideguchi, and S. P. Gorza, "Nonlinear optical interactions in silicon waveguides," *Nanophotonics*, vol. 6, no. 2, pp. 377–392 Nov. 2017.

[26] O. Boyraz, T. Indukuri, and B. Jalali, "Self-phase-modulation induced spectral broadening in silicon waveguides," *Opt. Express*, vol. 12, no. 5, pp. 829–834, 2004.

[27] L. Yin and G. P. Agrawal, "Impact of two-photon absorption on self-phase modulation in silicon waveguides," *Opt. Lett.*, vol. 32, no. 14, pp. 2031–2033, Jul. 2007.

[28] E.-K. Tien, X.-Z. Sang, F. Qing, Q. Song, and O. Boyraz, "Ultrafast pulse characterization using cross phase modulation in silicon," *Appl. Phys. Lett.*, vol. 95, no. 5, Aug. 2009, Art. no. 051101.

[29] X. Chen, N. C. Panoiu, and R. M. Osgood, "Theory of Raman-mediated pulsed amplification in silicon-wire waveguides," *IEEE J. Quantum Electron.*, vol. 42, no. 2, pp. 160–170, Feb. 2006.

[30] H.-S. Hsieh, K.-M. Feng, and M.-C.-M. Lee, "Study of cross-phase modulation and free-carrier dispersion in silicon photonic wires for mamyshev signal regenerators," *Opt. Express*, vol. 18, no. 9, pp. 9613–9621, Apr. 2010.

[31] H. Rong, A. Liu, R. Jones, O. Cohen, D. Hak, R. Nicolaescu, A. Fang, and M. Paniccia, "An all-silicon Raman laser," *Nature*, vol. 433, no. 7023, pp. 292–294, Jan. 2005.

[32] O. Boyraz and B. Jalali, "Demonstration of a silicon Raman laser," *Opt. Express*, vol. 12, no. 21, pp. 5269–5273, 2004.

[33] H. Hu, H. Ji, M. Galili, M. Pu, C. Peucheret, H. C. H. Mulvad, K. Yvind, J. M. Hvam, P. Jeppesen, and L. K. Oxenláwe, "Ultra-high-speed wavelength conversion in a silicon photonic chip," *Opt. Express*, vol. 19, no. 21, pp. 19886–19894, Oct. 2011.

[34] R. Salem, M. A. Foster, A. C. Turner, D. F. Geraghty, M. Lipson, and A. L. Gaeta, "Signal regeneration using low-power four-wave mixing on silicon chip," *Nature Photon.*, vol. 2, no. 1, pp. 35–38, Jan. 2008.

[35] A. Biberman, B. G. Lee, A. C. Turner-Foster, M. A. Foster, M. Lipson, A. L. Gaeta, and K. Bergman, "Wavelength multicasting in silicon photonic nanowires," *Opt. Express*, vol. 18, no. 17, pp. 18047–18055, Aug. 2010.

[36] S. Lavdas, J. B. Driscoll, H. Jiang, R. R. Grote, R. M. Osgood, and N. C. Panoiu, "Generation of parabolic similaritons in tapered silicon photonic wires: Comparison of pulse dynamics at telecom and mid-infrared wavelengths," *Opt. Lett.*, vol. 38, no. 19, pp. 3953–3956, Oct. 2013.

[37] C. Mei, F. Li, J. Yuan, Z. Kang, X. Zhang, B. Yan, X. Sang, Q. Wu, X. Zhou, K. Zhong, L. Wang, K. Wang, C. Yu, and P. K. A. Wai, "Comprehensive analysis of passive generation of parabolic similaritons in tapered hydrogenated amorphous silicon photonic wires," *Sci. Rep.*, vol. 7, no. 1, Dec. 2017, Art. no. 3814.

[38] S. Lavdas, J. B. Driscoll, R. R. Grote, R. M. Osgood, and N. C. Panoiu, "Generation and collision of optical similaritons in dispersion-engineered silicon photonic nanowires," *Proc. SPIE Nanoeng. Fabr., Properties, Opt., Devices*, vol. 8816, Sep. 2013, Art. no. 88160.

[39] C. Mei, K. Wang, J. Yuan, Z. Kang, X. Zhang, B. Yan, X. Sang, Q. Wu, X. Zhou, C. Yu, and G. Farrell, "Self-similar propagation and compression of the parabolic pulse in silicon waveguide," *J. Lightw. Technol.*, vol. 37, no. 9, pp. 1990–1999, May 2019.

[40] G. P. Agrawal, P. L. Baldeck, and R. R. Alfano, "Optical wave breaking and pulse compression due to cross-phase modulation in optical fibers," *Opt. Lett.*, vol. 14, no. 2, pp. 137–139, Jan. 1989.

[41] G. P. Agrawal, P. L. Baldeck, and R. R. Alfano, "Temporal and spectral effects of cross-phase modulation on copropagating ultrashort pulses in optical fibers," *Phys. Rev. A, Gen. Phys.*, vol. 40, no. 9, pp. 5063–5072, Nov. 1989.

[42] I.-W. Hsieh, X. Chen, J. I. Dadap, N. C. Panoiu, R. M. Osgood, Jr., S. J. McNab, and Y. A. Vlasov, "Cross-phase modulation-induced spectral and temporal effects on co-propagating femtosecond pulses in silicon photonic wires," *Opt. Express*, vol. 15, no. 3, pp. 1135–1146, 2007.

[43] D. K. Schroder, R. N. Thomas, and J. C. Swartz, "Free carrier absorption in silicon," *IEEE Trans. Electron Devices*, vol. 25, no. 2, pp. 254–261, Feb. 1978.

[44] G. W. Rieger, K. S. Virk, and J. F. Young, "Nonlinear propagation of ultrafast 1.5 μm pulses in high-index-contrast silicon-on-insulator waveguides," *Appl. Phys. Lett.*, vol. 84, no. 6, pp. 900–902, Feb. 2004.

[45] G. P. Agrawal, "Nonlinear fiber optics," in *Nonlinear Science at the Dawn of the Century*. Berlin, Germany: Springer, 2004.

[46] L. Zhang, A. M. Agarwal, L. C. Kimerling, and J. Michel, "Nonlinear group IV photonics based on silicon and germanium: From near-infrared to mid-infrared," *Nanophotonics*, vol. 3, nos. 4–5, pp. 247–268, Aug. 2014.

[47] P. E. Barclay, K. Srinivasan, and O. Painter, "Nonlinear response of silicon photonic crystal micresonators excited via an integrated waveguide and fiber taper," *Opt. Express*, vol. 13, no. 3, pp. 801–820, 2005.

[48] J. M. Dudley, G. Genty, and S. Coen, "Supercontinuum generation in photonic crystal fiber," *Rev. Modern Phys.*, vol. 78, no. 4, pp. 1135–1184, 2006.

CHAO MEI (Member, IEEE) received the B.S. degree in optical information science and technology from Harbin Engineering University, Harbin, China, in 2013, and the Ph.D. degree in optical engineering from the Beijing University of Posts and Telecommunication, Beijing, China, in 2019. He currently holds a postdoctoral position with the Max-Born Institute for Nonlinear Optics and Short Pulse Spectroscopy (MBI), Berlin, Germany, and cooperates with the University of Science and Technology Beijing (USTB), Beijing, China. His current research interest includes ultrafast optics, nonlinear optics, and nonlinear dynamics in optical devices and optical systems.

JINHUI YUAN (Senior Member, IEEE) received the Ph.D. degree in physical electronics from the Beijing University of Posts and Telecommunications (BUPT), Beijing, China, in 2011. He is currently a Professor with the Department of Computer and Communication Engineering, University of Science and Technology Beijing (USTB). He was selected as a Hong Kong Scholar at the Photonics Research Center, Department of Electronics and Information Engineering, The Hong Kong Polytechnic University, in 2013. He has published more than 200 articles in the academic journals and conferences. His current research interests include photonic crystal fibers, silicon waveguide, and optical fiber devices. He is the Senior Member of OSA.

FENG LI (Member, IEEE) received the B.S. and Ph.D. degrees from the University of Science and Technology of China, Hefei, China, in 2001 and 2006, respectively. After that, he joined The Hong Kong Polytechnic University as a Postdoctoral Fellow. He is currently a Research Fellow with The Hong Kong Polytechnic University. His research interests include fiber lasers, especially multiwavelength lasers and mode locked lasers, nonlinear fiber optics, supercontinuum generation, and nonlinear dynamics in optical devices and optical systems.

XIAN ZHOU received the Ph.D. degree in electromagnetic field and microwave technology from the Beijing University of Posts and Telecommunications (BUPT), Beijing, China, in 2011. She is currently an Associate Professor with the Department of Computer and Communication Engineering, University of Science & Technology Beijing (USTB). She is also a Hong Kong Scholar with the Photonics Research Centre, Department of Electronic and Information Engineering, The Hong Kong Polytechnic University. Her research interests are focused on high-speed optical communications, short reach communications, and digital signal processing.

QIANG WU received the B.S. degree from the Beijing Normal University, Beijing, China, in 1996, and the Ph.D. degree from the Beijing University of Posts and Telecommunications, Beijing, China, in 2004. From 2004 to 2006, he was a Senior Research Associate with the City University of Hong Kong. From 2006 to 2008, he took up a research associate post in Heriot-Watt University, U.K. From 2008 to 2014, he was a Stokes Lecturer with the Photonics Research Centre, Dublin Institute of Technology, Ireland. He is currently an Associate Professor with Northumbria University, U.K., and also a Honorary Professor with NanChang Hangkong University, China. His research interests include photonics devices and fiber optic sensing.

BINBIN YAN received the B.S. and M.S. degrees from the Beijing University of Posts and Telecommunications (BUPT), Beijing, China, in 2003 and 2005, respectively, and the Ph.D. degree from BUPT, in 2009. She is currently with BUPT as a Lecturer. Her research interests include photonic devices and fiber optic sensing.

KUIRU WANG received the B.S. and M.S. degrees from the Beijing University of Posts and Telecommunications (BUPT), Beijing, China, in 1984 and 1990, respectively, and the Ph.D. degree from BUPT, in 2009. She is currently with BUPT as a Professor. Her current research interests include optical fiber communications and photonic devices.

KEPING LONG (Senior Member, IEEE) received the M.S. and Ph.D. degrees from UESTC, in 1995 and 1998, respectively. He was an Associate Professor with the Beijing University of Posts and Telecommunications. From July 2001 to November 2002, he was a Research Fellow with the ARC Special Research Centre for Ultra Broadband Information Networks (CUBIN), University of Melbourne, Australia. He is currently a Professor and the Dean with the School of Computer and Communication Engineering, University of Science & Technology Beijing (USTB). He has published more than 200 articles, 20 keynotes, and invited talks. His research interests are optical Internet technology, new generation network technology, wireless information networks, value-added service, and secure network technology. He is a member of the Editorial Committee of Sciences in China Series F and China Communications. He was awarded the National Science Fund Award for Distinguished Young Scholars of China in 2007 and selected as the Chang Jiang Scholars Program Professor of China in 2008. He has also been a TPC and ISC member for COIN, IEEE IWCN, ICON, and APOC, and an Organizing Co-Chair of IWCMC 2006, TPC Chair of COIN from 2005 to 2008, and a TPC Co-Chair of COIN from 2008 to 2010.

GERALD FARRELL received the Graduate degree(Hons.) in electronic engineering from the University College Dublin, Dublin, Ireland, in 1979, and the Ph.D. degree from Trinity College Dublin, Dublin, Ireland, for research in all-optical synchronization using self-pulsating laser diodes. From 1997 to 2003, he was the Director of the startup company PX Instrument Technology, focusing on optical fiber system test and measurement systems. He spent a number of years as a Communications Systems Design Engineer developing optical fiber trans-mission systems before joining the Dublin Institute of Technology (DIT), Dublin, Ireland. He has been the Head of the School of Electronic and Communications Engineering, DIT, since 2001. He is currently the Founder and the Director of the Photonics Research Centre, DIT. He has more than 300 publications in the area of photonics. His current research interests include several areas of optical sensing including FBG interrogation systems, the modeling and applications of fiber bent loss to optical sensing, SMS and other fiber structure for sensing applications, PCF sensors for environmental sensing and for sensing strain in composite materials and medical devices, LC infiltrated PCF sensor, and microfiber and nanowire sensors for biosensing.

CHONGXIU YU graduated from the Beijing University of Posts and Telecommunications (BUPT), Beijing, China, in 1969. She is currently with BUPT as a Professor. She is engaged in university education and research work and has been the Principal Investigator of many projects supported by China 863 plan, the National Natural Science Foundation and the National Ministry of Science Technology, and so on. Up to now, she has published more than 300 articles. Her research interests are the optical fiber communication, photonic switching, and optoelectronics technology and its applications. She is a member of the Chinese Institute of Communication, the Committee of Fiber Optics and Integral Optics, and the Chinese Optical Society.